European Journal of Environmental and Civil Engineering

ISSN: (Print) (Online) Journal homepage: https://www.tandfonline.com/loi/tece20

Shear banding in unsaturated geomaterials through a strong nonlocal hydromechanical model

Shashank Menon & Xiaoyu Song

To cite this article: Shashank Menon & Xiaoyu Song (2020): Shear banding in unsaturated geomaterials through a strong nonlocal hydromechanical model, European Journal of Environmental and Civil Engineering, DOI: 10.1080/19648189.2020.1797889

To link to this article: https://doi.org/10.1080/19648189.2020.1797889

Published online: 30 Jul 2020.

EUROPEAN JOURNAL OF ENVIRONMENTAL AND CIVIL ENGINEERING
https://doi.org/10.1080/19648189.2020.1797889

Shear banding in unsaturated geomaterials through a strong nonlocal hydromechanical model

Shashank Menon and Xiaoyu Song

Engineering School of Sustainable Infrastructure & Environment, University of Florida, Gainesville, FL, USA

ABSTRACT

We present a strong nonlocal hydromechanical model formulated based on state-based peridynamics for simulating strain localisation in unsaturated geomaterials. The governing equations are integro-differential equations in which length scales are assumed for both the skeleton deformation and pore fluid flow. Recently proposed hydromechanical correspondence principle is adopted to implement the classical local constitutive model for the solid skeleton, and the generalised Darcy's law for unsaturated water flow into the nonlocal hydromechanical model. Numerical simulations of shear bands in unsaturated geomaterials were conducted to investigate the effect of the hydromechanical length scale and the mechanical loading rate on the formation of shear bands. The numerical results have shown that both the deformation and pore water pressure are concentrated in the shear bands with a finite thickness. The numerical results have demonstrated that both the hydromechanical length scale and the mechanical loading rate affect the formation of shear bands in unsaturated geomaterials and the peak value of the load capacity of unsaturated geomaterials.

ARTICLE HISTORY
Received 30 December 2019
Accepted 29 June 2020

KEYWORDS
Shear banding; unsaturated geomaterials; strong nonlocal; hydromechanical model; coupled

1. Introduction

Shear banding or strain localisation is a significant issue in geomaterials (e.g. clay and sand) under variably saturated conditions because it signifies the failure of such materials (e.g. Borja, Song, Rechenmacher, et al., 2013; Chang et al., 2009; Jrad et al., 2012; Song, 2014; Song, Wang, & Ye, 2018). Shear banding in unsaturated geomaterials is of interest in a broad spectrum of fields, including geophysics, petroleum engineering (Li & Laloui, 2017), nuclear waste storage (Pardoen et al., 2015), and geotechnical engineering (Likos et al., 2019; Song et al., 2017; Song, Wang, & Bate, 2018; Wang & Song, 2020). Unsaturated geomaterials are three-phase porous media that consist of a solid skeleton and two immiscible fluid phases, i.e. pore water and pore air. In unsaturated geomaterials, the pore water pressure is under tension. The difference between pore air pressure and pore water pressure is called matric suction. The degree of saturation is defined as the ratio between the volume of pore water and the total volume of pore space. Both the matric suction and degree of saturation are critical variables in modeling unsaturated geomaterials (Lu & Likos, 2004). For instance, unsaturated soil slope failure can be triggered by the heavy rain-fall induced reduction of matric suction and increase of the degree of saturation (Askrinejad et al., 2012). It has also been demonstrated that the heterogeneities of matric suction and the degree of saturation of the water phase can trigger shear bands in unsaturated soils (Song & Borja, 2014a). Physically, shear banding in unsaturated geomaterials involves the intricate coupling processes of the solid deformation and unsaturated fluid flow (Song, 2017). In the localised failure zone, not only the

CONTACT Xiaoyu Song xysong@ufl.edu Engineering School of Sustainable Infrastructure & Environment, University of Florida, Gainesville, FL 32611, USA

deformation of the solid phase but also the negative fluid pressure or matric suction can be concentrated in narrow banded zones with a finite thickness provided the general plastic behavior of the geomaterial is dilatant.

Hence, a fully coupled mathematical model is needed to incorporate the complex multiphysical processes for modeling shear banding in unsaturated geomaterials. The mixed finite element method has been used to simulate shear banding in unsaturated geomaterials (Borja, Song, & Wu, 2013; Song & Borja, 2014b). However, these studies have been focused on the inception of shear banding in unsaturated geomaterials triggered by material heterogeneities (e.g. porosity and the degree of saturation). It is well recognised the thickness of shear bands in geomaterials is related to the microstructure of geomaterials (e.g. grain size) (e.g. Andò et al., 2012; Desrues et al., 1996). For the numerical simulations with the finite element method, the thickness of shear bands strongly depends on the finite element size because of the mesh sensitivity issue. Numerical models based on Cosserat theory and second gradient theory (e.g. Ehlers et al., 2003; Pardoen et al., 2015; Rattez, 2017) have been developed to simulate geomaterials under saturated and unsaturated conditions. In general, a length scale is needed to regularise the finite element model for simulating strain localisation. For modeling the coupled fluid flow and solid deformation in unsaturated geomaterials, there is a natural length scale related to Darcy's law under the dynamic condition. Numerical simulations have demonstrated that the length scale related to fluid flow may disappear under the quasi-static condition (Zhang & Schrefler, 2004).

The peridynamics theory which is nonlocal is a reformulation of the classical continuum mechanics to deal with discontinuities (Silling, 2000; Silling et al., 2007). Peridynamics is formulated based on the spatial integral equation in lieu of partial differential equations, which are not defined at discontinuities, e.g. shear bands. The peridynamic governing equations are defined at shear bands, and material failure is part of the peridynamic constitutive models. Hence, peridynamics can model the inception and propagation of shear bands with arbitrary paths without a special treatment to guide the propagation of shear bands. Peridynamics has been applied to model shear banding in unsaturated soils under drained condition (or uncoupled) and desiccation cracking (Song & Khalili, 2019; Song & Menon, 2019; Menon & Song, 2019). Song and Khalili (2019) formulated and implemented a correspondence peridynamics constitutive model for unsaturated soils through the peridynamic constitutive correspondence principle. Song and Menon (2019) developed a nonlocal chemo-hydromechanical model for unsaturated soils through state-based peridynamics. It shall be noted that the numerical simulations in the literature (e.g. Song & Khalili, 2019; Song & Menon, 2019) were conducted under drained conditions, and the coupling effect of the unsaturated fluid flow was not explicitly accounted for.

In this article, we present a strong nonlocal coupled hydromechanical model formulated based on peridynamics for simulating strain localisation in unsaturated geomaterials. The governing equations are integro-differential equations in which length scales are assumed for both the skeleton deformation and pore fluid flow. Recently proposed hydromechanical correspondence principle is adopted to implement the classical local constitutive model for the solid skeleton, and the generalised Darcy's law for unsaturated water flow into the nonlocal hydromechanical model. Numerical simulations of shear bands in unsaturated geomaterials were conducted to investigate how the spatial length scale and the mechanical loading rate impact the formation of shear bands. The numerical results showed that both the deformation and pore water pressure are concentrated in the shear bands with a finite thickness. The numerical results have demonstrated that both the spatial length scale and the mechanical loading rate affect the formation of shear bands and the load capacity of unsaturated geomaterials. The remainder of the article is structured as follows. Section 2 presents the nonlocal hydromechanical model. Section 3 deals with the numerical simulations of strain localisation in unsaturated geomaterials and the impact of the length scale and mechanical loading rate on the formation of shear bands in unsaturated geomaterials, followed by a summary in Section 4.

2. Nonlocal hydromechanical model

This section presents a strong nonlocal hydromechanical model cast in the framework of state-based peridynamics through the recently proposed hydromechanical correspondence principle (Song & Silling, 2019). State-based peridynamics is a nonlocal reformulation of classical continuum mechanics in terms of integro-differential equations. In this formulation, it is assumed that the porous media are composed of material points that interact with each other in a nonlocal region called the 'horizon'. Passive atmospheric

pressure is assumed for the pore air pressure in the mathematical formulation, as usually adopted in geotechnical engineering (Zienkiewicz et al., 1999). Thus, each material point has four degrees of freedom, e.g. three for displacement and one for pore water pressure. In line with the classic poromechanics, solid skeleton is described by Lagrangian coordinate system, and pore water is described by the relative Eulerian coordinate system with respect to the solid skeleton. Next, we first introduce the governing equations for the coupled hydromechanical process. Then we introduce the non-local constitutive laws for the solid skeleton and fluid flow through the hydromechanical correspondence principle.

2.1. Governing equations

The governing equations consist of the linear momentum balance equation of the mixture and the mass balance equation of the fluid phase coupled with the deformation of the solid skeleton. Both equations will be formulated through the state concept of the state-based peridynamics (Silling et al., 2007). For the solid skeleton, let $\boldsymbol{x}$ be the position vector of a material point in the problem domain, and $\boldsymbol{x}'$ be the position vector of any material point within its horizon in the reference configuration. Furthermore, let $\boldsymbol{y}(\boldsymbol{x})$ and $\boldsymbol{y}'(\boldsymbol{x})$ be the position vectors of material points $\boldsymbol{x}$ and $\boldsymbol{x}'$ respectively in the deformed configuration. The reference position vector state and the deformation vector state for the solid skeleton at material point $\boldsymbol{x}$ are defined as

$$\boldsymbol{X}\langle\boldsymbol{\xi}\rangle = \boldsymbol{\xi} = \boldsymbol{x}' - \boldsymbol{x}, \tag{1}$$

$$\boldsymbol{Y}\langle\boldsymbol{\xi}\rangle = \boldsymbol{y}(\boldsymbol{x}') - \boldsymbol{y}(\boldsymbol{x}), \tag{2}$$

where the angle bracket denotes the bond that the vector state is imposed on. Given the deformation state, the effective force state of the skeleton can be determined by the constitutive model (see subsection 2.2). It is noted that the effective force state also depends on the negative pressure (or suction). Let $\bar{\boldsymbol{T}}$ be the effective force state of the soil skeleton. Following the generalised effective stress concept in unsaturated soil mechanics (Lu et al., 2010), the total force state of the mixture can be decomposed into the effective force state of the skeleton and the pore water force state as follows:

$$\boldsymbol{T} = \bar{\boldsymbol{T}} - S_r\boldsymbol{T}_w, \tag{3}$$

where S_r is the degree of saturation which can be determined by soil water retention curve (Cao et al., 2018) and $\boldsymbol{T}_w$ is the force state of the pore water (negative for unsaturated soils) which is defined in Section 2.2. Then the linear momentum balance equation of the mixture at material point $\boldsymbol{x}$ under quasi-static condition is written as

$$\int_{H_x} \left(\boldsymbol{T}\langle\boldsymbol{\xi}\rangle - \boldsymbol{T}'\langle-\boldsymbol{\xi}\rangle\right) dV_{x'} + [(1-\phi)\rho_s + \phi S_r\rho_w]\boldsymbol{g} = 0, \tag{4}$$

where $\boldsymbol{T}$ is the total force vector state at the point $\boldsymbol{x}$ acting on the bond $\boldsymbol{\xi}$, $\boldsymbol{T}'$ is the total force vector state at the point $\boldsymbol{x}'$ acting on the bond $-\boldsymbol{\xi}$, H_x is the horizon of material point $\boldsymbol{x}$, ϕ is porosity, ρ_s and ρ_w are the intrinsic density of the solid and the water respectively, and $\boldsymbol{g}$ is the gravity acceleration.

Let p_w and p'_w are the pore water pressures at the material points $\boldsymbol{x}$ and $\boldsymbol{x}'$, respectively. We define the pressure potential scalar state at material points $\boldsymbol{x}$ in the current configuration associated with $\boldsymbol{\xi}$ respectively as follows:

$$\Phi_w\langle\boldsymbol{\xi}\rangle = p'_w - p_w, \tag{5}$$

Let Q_w and Q'_w be the mass flow scalar states of the pore water phase with respect to the solid skeleton at the material points $\boldsymbol{x}$ and $\boldsymbol{x}'$, respectively. Let $\dot{\mathcal{V}}$ and $\dot{\mathcal{V}}'$ be the rate of change of volume in the solid phase at the material points $\boldsymbol{x}$ and $\boldsymbol{x}'$, respectively. Then, the peridynamic equation of mass balance for material point $\boldsymbol{x}$ can be written as

$$\phi\frac{dS_r}{dt} + \frac{\phi S_r}{K_w}\frac{dp_w}{dt} + S_r\int_{H_x}\left(\dot{\mathcal{V}} - \dot{\mathcal{V}}'\right)dV' + \frac{1}{\rho_w}\int_{H_x}\left(Q_w - Q'_w\right)dV' = 0, \tag{6}$$

where K_w is the bulk modulus of pore water, and the third term represents the nonlocal volume change of the solid phase, which is in line with how the state-based peridynamics approximates the divergence operator. Note that Equations (4) and (6) are general in the sense that the constitutive models for the

solid skeleton and the pore water phase are not defined yet. Next, we define the total force state and the mass flow state in terms of the local constitutive models for the solid deformation and the fluid flow.

2.2. Hydromechanical correspondence principle

We define the approximate nonlocal deformation gradient for the solid skeleton and the approximate nonlocal water pressure gradient through the hydromechanical correspondence principle (Song & Silling, 2019), which extends the original constitutive correspondence principle for the solid material (Silling et al., 2007). The correspondence principle allows the incorporation of the local constitutive model in the framework of the state-based peridynamics. The approximate nonlocal deformation gradient and nonlocal fluid pressure gradient at material point $\boldsymbol{x}$ of the mixture are respectively defined as

$$\bar{\boldsymbol{F}} = \left(\int_{H_x} \omega\langle\boldsymbol{\xi}\rangle \boldsymbol{Y}\langle\boldsymbol{\xi}\rangle \otimes \boldsymbol{X}\langle\boldsymbol{\xi}\rangle \; dV'\right)\boldsymbol{K}^{-1}, \tag{7}$$

$$\overline{\nabla\Phi}_w = \left(\int_{H_x} \omega\langle\boldsymbol{\xi}\rangle \Phi_w \boldsymbol{X}\langle\boldsymbol{\xi}\rangle dV'\right)\boldsymbol{K}^{-1}, \tag{8}$$

where $\omega\langle\boldsymbol{x}\rangle$ is a weighting function, $\otimes$ is the tensor product operator, and $\boldsymbol{K}$ is the shape tensor which is defined as

$$\boldsymbol{K} = \int_{H_x} \omega\langle\boldsymbol{\xi}\rangle(\boldsymbol{\xi}\otimes\boldsymbol{\xi})dV'. \tag{9}$$

Given the deformation gradient of the solid skeleton, the effective stress $\bar{\boldsymbol{\sigma}}$ of the solid skeleton can be calculated through the classical constitutive model. In this article, the material model in Song and Khalili (2019) is used to model the solid skeleton. Then through the correspondence principle the total force state at the material point $\boldsymbol{x}$ can be written as

$$\boldsymbol{T} = \omega\boldsymbol{\sigma}J\bar{\boldsymbol{F}}^{-T}\boldsymbol{K}^{-1}\boldsymbol{\xi}, \tag{10}$$

where J is the determinant of the nonlocal deformation gradient $\bar{\boldsymbol{F}}$ and $\boldsymbol{\sigma} = (\bar{\boldsymbol{\sigma}} - S_r p_w \boldsymbol{1})$ is the total stress.

Similarly, given the nonlocal water pressure gradient, the fluid flux vector $\boldsymbol{q}_w$ at material point $\boldsymbol{x}$ can be determined by the generalised Darcy's law as

$$\boldsymbol{q}_w = -k_w^r \frac{\kappa}{\mu_w}\overline{\nabla\Phi}_w = -k_w^r \frac{\kappa}{\mu_w}\left(\int_{H_x} \omega\Phi_w \boldsymbol{X}\langle\boldsymbol{\xi}\rangle dV'\right)\boldsymbol{K}^{-1}, \tag{11}$$

where k_w^r is the relative permeability (Niu et al., 2020) which is determined by water retention curve (Van Genuchten, 1980), κ is the isotropic permeability, and μ_w is the viscosity of water. The fluid flow state at material point $\boldsymbol{x}$ is defined as

$$Q_w = \omega\rho_w J\boldsymbol{q}_w\boldsymbol{K}^{-1}\boldsymbol{\xi}. \tag{12}$$

Given the total force state in terms of the total stress tensor, the linear momentum balance at the material point $\boldsymbol{x}$ can be written as

$$\int_{H_x}\left[\left(\omega\boldsymbol{\sigma}J\bar{\boldsymbol{F}}^{-T}\boldsymbol{K}^{-1}\boldsymbol{\xi}\right) - \left(\omega\boldsymbol{\sigma}'J\bar{\boldsymbol{F}}^{-T}\boldsymbol{K}^{-1}\boldsymbol{\xi}'\right)\right]dV' + [\rho_s(1-\phi) + \rho_w\phi S_r]\boldsymbol{g} = \boldsymbol{0} \tag{13}$$

where $\boldsymbol{\sigma}$ and $\boldsymbol{\sigma}'$ are the total stress tensors at the material points $\boldsymbol{x}$ and $\boldsymbol{x}'$, respectively. The rate of volume change of the solid skeleton in the framework of state-based peridynamics at the material point $\boldsymbol{x}$ can be written as

$$\int_{H_x}(\dot{\mathcal{V}} - \dot{\mathcal{V}}')dV' = \int_{H_x}\left(\omega\dot{\boldsymbol{Y}}\boldsymbol{K}^{-1}\boldsymbol{\xi} - \omega\dot{\boldsymbol{Y}}'\boldsymbol{K}^{-1}\boldsymbol{\xi}'\right)dV'. \tag{14}$$

where $\dot{\boldsymbol{Y}}$ and $\dot{\boldsymbol{Y}}'$ are the rate of the deformation states at the material points $\boldsymbol{x}$ and $\boldsymbol{x}'$, respectively.

Then, assuming that water is incompressible the mass balance equation of the mixture can be written as

$$\begin{aligned}\phi\frac{dS_r}{dt} + S_r\int_{H_x}\left(\omega\dot{\boldsymbol{Y}}\boldsymbol{K}^{-1}\boldsymbol{\xi} - \omega\dot{\boldsymbol{Y}}'\boldsymbol{K}^{-1}\boldsymbol{\xi}'\right)dV' \\ + \int_{H_x}\left(\omega J\boldsymbol{q}_w\boldsymbol{K}^{-1}\boldsymbol{\xi} - \omega J\boldsymbol{q}_w'\boldsymbol{K}^{-1}\boldsymbol{\xi}'\right)dV' = 0\end{aligned} \tag{15}$$

The governing equations are solved through the Lagrangian meshfree method originally proposed by Silling and Askari (2005). A general discussion of meshfree methods is beyond the scope of the article.

3. Numerical simulations

In this section, we investigate the impact of length scales and the loading rate on the formation of shear banding in unsaturated geomaterials through two-dimensional compression tests under constant lateral confining pressure.

We first conduct a base simulation of the formation of shear bands in unsaturated soils. Then numerical results are presented to study the impact of length scale and loading rate on shear banding. All numerical simulations are conducted under two-dimensional condition. The correspondence plastic model for unsaturated soils in Song and Khalili (2019) is adopted for the solid skeleton. In this model, the yield surface f is determined by

$$f(p', q, \bar{p}_c) = \frac{q^2}{M^2} + (p' - \bar{p}_c)p' \leq 0, \tag{16}$$

where p' is the effective mean stress, q is the equivalent shear stress, M is the slope of the critical state line, and $\bar{p}$ is the apparent effective preconsolidation pressure. As a hardening law, $\bar{p}_c$ is expressed as

$$\bar{p}_c = -\exp(a_1)(-p_c)^{a_2}, \tag{17}$$

where a_1 and a_2 are two variables that evolve with matric suction and the degree of saturation (Borja, 2004; Song & Khalili, 2019), and p_c is the apparent preconsolidation pressure under saturated condition which evolves with plastic volumetric strain. The rate form of p_c reads as,

$$\dot{p}_c = \frac{-p_c}{\lambda - \kappa}\dot{\varepsilon}_v^p, \tag{18}$$

where λ and κ are the swelling index and the compression index, respectively, and $\dot{\varepsilon}_v^p$ is the rate form of the plastic volumetric strain of the solid skeleton. The input material parameters are: the bulk modulus $K = 34$ MPa, the shear modulus $G = 25$ MPa, the swelling index $\kappa = 0.03$, the critical state line slope $M = 1.0$, the compression index $\lambda = 0.11$, the soil density $\rho_s = 2500\,\text{kg/m}^3$, the water density $\rho_w = 1000\,\text{kg/m}^3$, the initial porosity $\phi = 0.5$, and the saturated permeability is 1×10^{-7} m/s. The soil-water retention curve and the relative permeability of water are assumed as follows (Van Genuchten, 1980).

$$S_r = \left[1 + (s/s_a)^n\right]^{-m}, \tag{19}$$

$$k_r = \sqrt{S_r}\left[1 - (1 - S_r^{1/m})^m\right]^2, \tag{20}$$

where s is matric suction, and s_a, n and m are material parameters. For all numerical simulations below, we assume $s_a = 10$ kPa, $n = 2.0$ and $m = 0.5$.

Figure 1 presents the geometry of the unsaturated soil specimen, boundary conditions, and loading protocol. The specimen (in blue) has a rectangular cross-section with dimensions 10 cm $\times$ 20 cm and 0.4 cm thickness. Fictitious boundaries (in grey) are used to apply the boundary conditions. The problem domain is discretised into 2500 material points with $\Delta x = 0.4$ cm. The horizon $\delta = 0.8$ cm. The bottom is fixed, and fluid-flow is prohibited on all boundaries of the specimen. For the initial state, mean effective stress is -100 kPa, suction is 20 kPa and a saturated preconsolidation pressure $p_c = -120$ kPa. The lateral confining pressure (equivalent total stress is -87 kPa) is applied through a linear ramp function in 1 s. Here, the lateral confining pressure is determined through the effective stress concept, i.e. the effective stress plus matric suction multiplied by the degree of saturation. From t = 1 s, the top boundary of the specimen is compressed in 1500 s with a rate $v_y = 0.006$ mm/s. The total displacement of the top boundary is 9 mm.

Figure 2 plots the reaction force versus the applied vertical strain. Figures 3–5 show the contours of plastic shear strain (the second invariant of deviatoric plastic strain tensor), plastic volume strain, and water pressure superimposed on the deformed configuration at three vertical strains, respectively. The results in Figures 3 and 4 show that two conjugate shear bands have developed in the specimen. The comparison of Figures 4 and 5 shows that the dilative shear band caused the matric suction in the shear

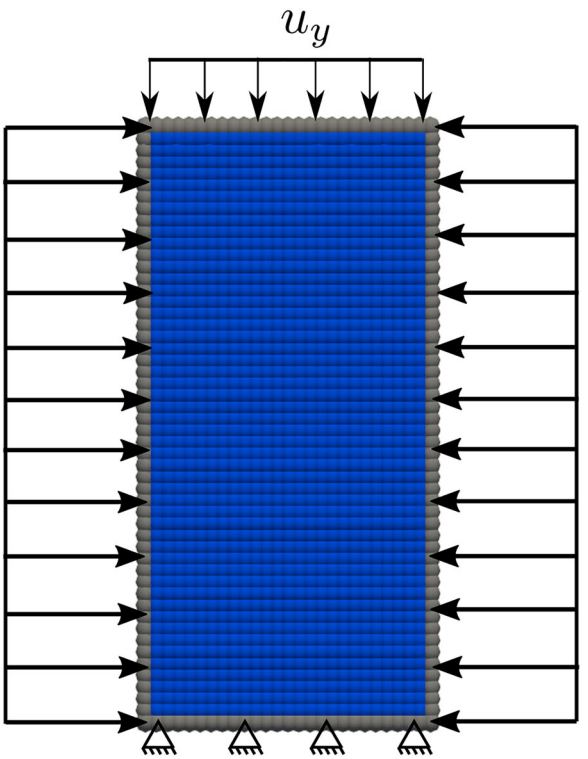

Figure 1. Model set-up and boundary and loading conditions.

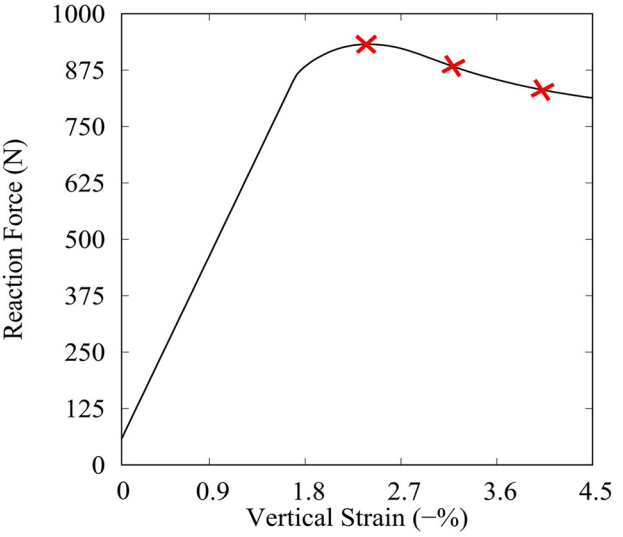

Figure 2. Reaction force vs. vertical strain. Note: markers are at vertical strains of 2.36%, 3.23%, and 4.0%.

band higher than that outside the shear band. The results in Figure 5 show that the pore water pressure does not change a lot, which is due to the choice of loading rates versus permeability.

3.1. Effect of length scales

This part concerns the effect of the length scale on shear banding. We rerun the base simulation with two additional horizons: $\delta = 10\,\text{mm}$ and $\delta = 12\,\text{mm}$. We compare the numerical results generated with

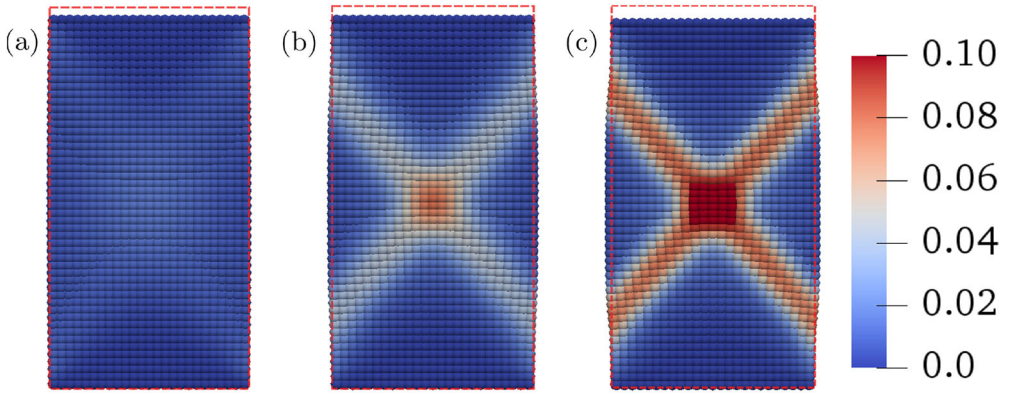

Figure 3. Contours of plastic shear strain at vertical strains of (a) 2.36%, (b) 3.23%, and (c) 4.0%, respectively.

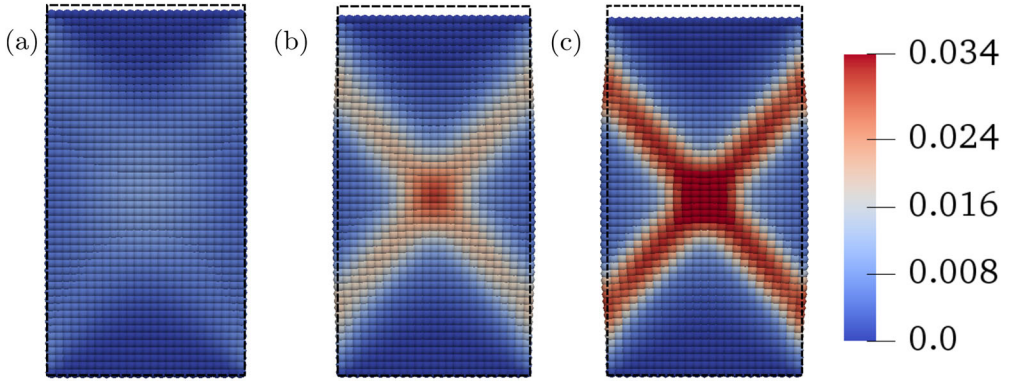

Figure 4. Contours of plastic volume strain at vertical strains of (a) 2.36%, (b) 3.23%, and (c) 4.0%, respectively.

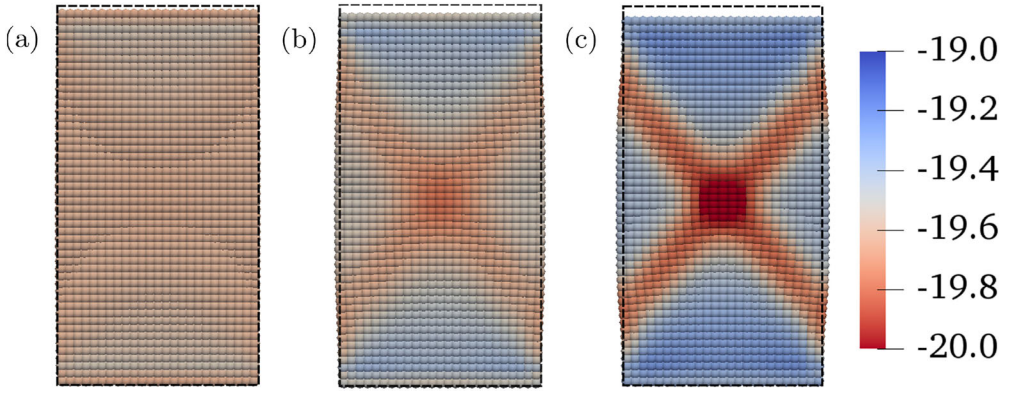

Figure 5. Contours of water pressure at vertical strains of (a) 2.36%, (b) 3.23%, and (c) 4.0%, respectively.

these two horizons and the base simulation. Figure 6 plot the reaction force vs. the applied vertical strain for all three cases. The loading curves show that the length scale does not affect the reaction force in the elastic deformation regime while it affects the reaction force in the post-localisation regime. Contours of the plastic shear and volumetric strains and water pressure are presented at two load steps. The first corresponds to the peak applied load, and the second is in the post-localisation regime. Both load steps (i.e. vertical strains) are represented by vertical dashed lines in Figure 6. For all three cases, the loading curves are almost identical in the elastic deformation range of the specimen. The results in the figure

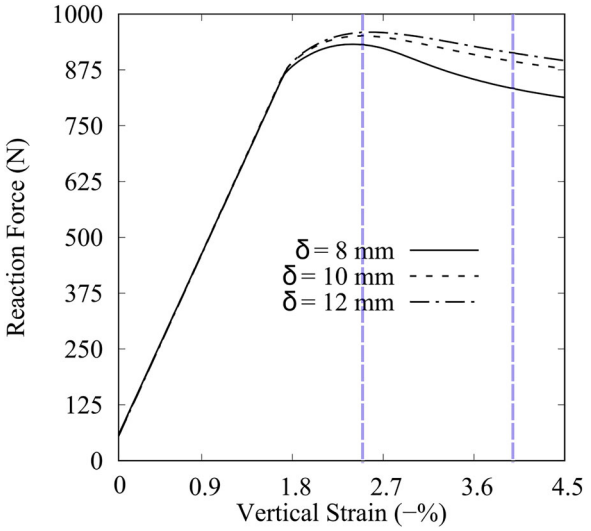

Figure 6. Reaction force vs. vertical strain for $\delta = 8$ mm, $\delta = 10$ mm, and $\delta = 12$ mm, respectively.

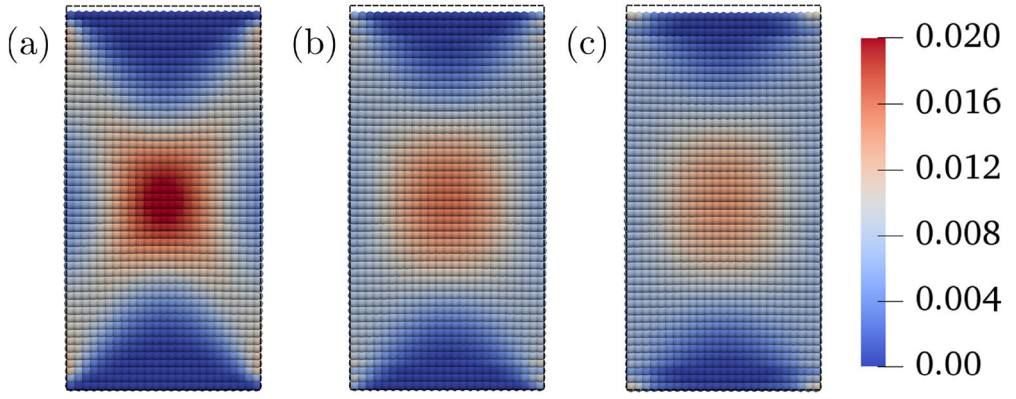

Figure 7. Contours of equivalent plastic shear strain at the peak applied load for (a) $\delta = 8$ mm, (b) $\delta = 10$ mm, and (c) $\delta = 12$ mm, respectively.

show that the chosen horizon or the length scale impacts the maximum loading capacity of the specimen. For instance, the simulation with a larger horizon generates a higher peak load capacity.

Figures 7 and 8 portray the contours of equivalent plastic shear strain at the peak applied load and in the post-localisation regime as denoted in Figure 6, respectively. Similarly, Figures 9 and 10 present the contours of plastic volumetric strains at both load steps, respectively. The results in these figures demonstrate that the length scale impacts both the inception and propagation of shear bands. For instance, the comparison of Figures 7 and 8 shows that the smaller length scale generates a larger magnitude of shear strains in the localised deformation zone at the same load steps. This is corroborated by the loading capacity curves in Figure 6. For the simulation with $\delta = 12$ mm, the plastic strain is concentrated at the center of the specimen. It may be concluded that the magnitude of plastic strain in the shear band is correlated to the spatial length scale. The contours of plastic volumetric strains in Figures 9 and 10 show that the shear bands are dilative ones in that the plastic volumetric strain is positive on the inception of shear bands and in the post-localisation regime which is due to the specimen being highly over-consolidated.

Figures 11 and 12 present the contours of water pressure superimposed on the deformed configuration at the pre-defined two load steps for all three cases. Cases (a), (b) and (c) stand for the simulations with $\delta = 8$ mm, 10 mm, and 12 mm, respectively. At the peak applied load step, despite the disparity in

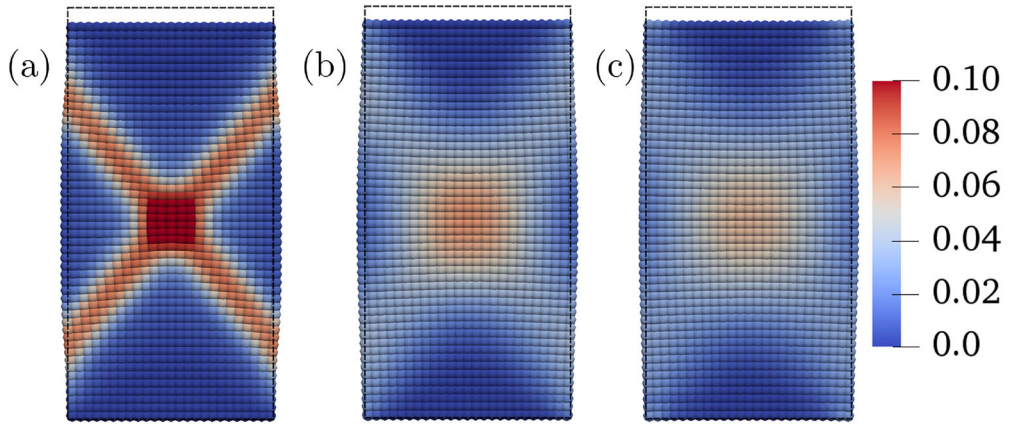

Figure 8. Contours of equivalent plastic shear strain in the post-localisation regime: (a) $\delta = 8$ mm, (b) $\delta = 10$ mm, and (c) $\delta = 12$ mm, respectively.

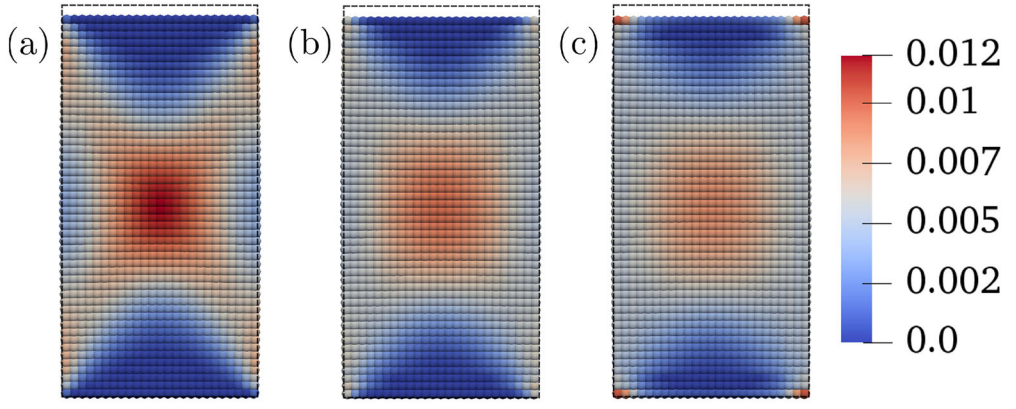

Figure 9. Contours of plastic volumetric strain at the peak applied load for (a) $\delta = 8$ mm, (b) $\delta = 10$ mm, and (c) $\delta = 12$ mm, respectively.

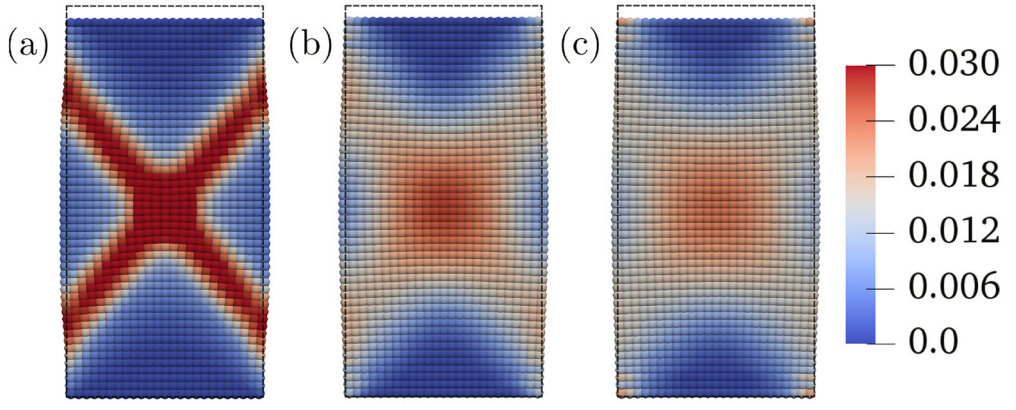

Figure 10. Contours of plastic volumetric strains in the post-localisation regime for (a) $\delta = 8$ mm, (b) $\delta = 10$ mm, and (c) $\delta = 12$ mm, respectively.

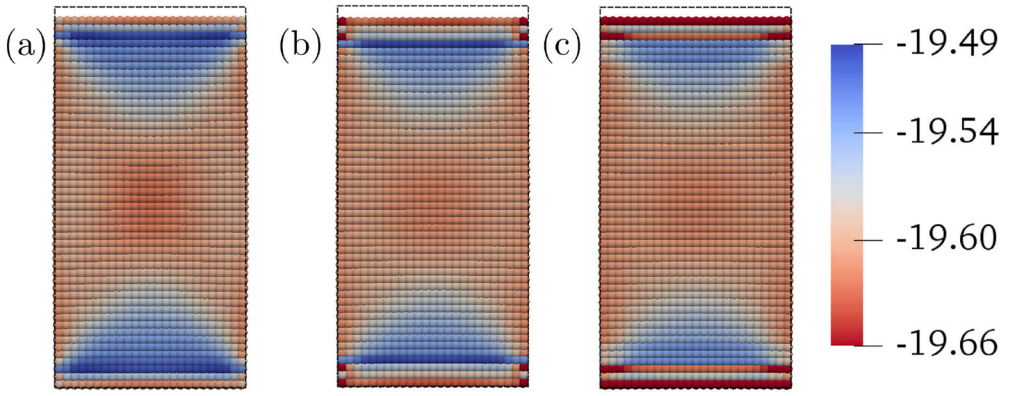

Figure 11. Contours of water pressure (Unit: kPa) at the peak applied load for (a) $\delta = 8$ mm, (b) $\delta = 10$ mm, and (c) $\delta = 12$ mm, respectively.

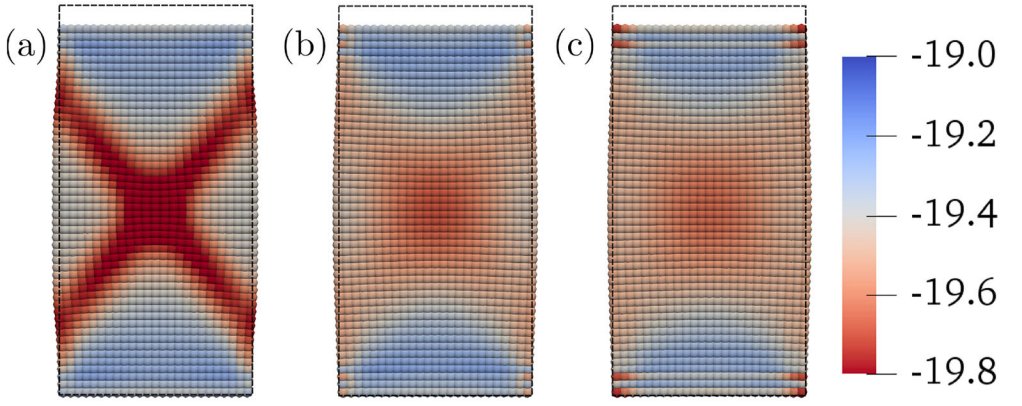

Figure 12. Contours of water pressure (Unit: kPa) in the post-localisation regime for (a) $\delta = 8$ mm, (b) $\delta = 10$ mm, and (c) $\delta = 12$ mm, respectively.

predicted plastic deformation, water pressure is largely identical for all three cases. However, this does not hold in the post-localisation regime. In the post-localised regime, Case (a) predicts a well defined localised zone of negative water pressure (i.e. matric suction) whereas Cases (b) and (c) show that negative water pressure have localised in wider conjugate zones. This may be interpreted by the fact that the simulations using a smaller length scale cause larger plastic volumetric strains (Figure 10) in the shear bands, which lead to the greater value of matric suction predicted by Case (a) in the post-localisation regime. For Cases (b) and (c) in Figure 12, the numerical results show smaller plastic volumetric strains and consequently smaller changes in negative water pressure or matric suction in the localised zone. It is evident that the length scale impacts both the solid deformation and fluid flow and the localised zone of both fields.

3.2. Effect of loading rates

This part deals with the influence of loading rates on the formation of shear bands. We report the numerical results for the same vertical compression with three loading rates. The three loading rates are (a) $v_y = 0.003$ mm/s, (b) $v_y = 0.006$ mm/s and (c) $v_y = 0.009$ mm/s. The total vertical strain is 4.5% for the three cases. Figure 13 plots the reaction force over the vertical strain generated by the simulations with the three loading rates. The results in Figure 13 show that the loading curves are almost identical in the elastic deformation regime, and then they start diverging when plastic deformation occurs. Furthermore, the loading rate also affects the peak reaction force. For instance, the peak reaction force increases with the increase of the loading rate. Next, we compare the results of the plastic shear and

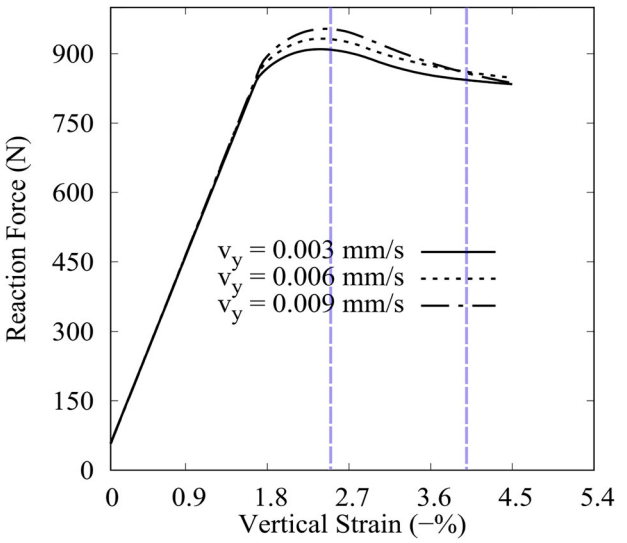

Figure 13. Reaction force versus vertical strain for three loading rates $v_y = 0.003$ mm/s, $v_y = 0.006$ mm/s, and $v_y = 0.009$ mm/s, respectively.

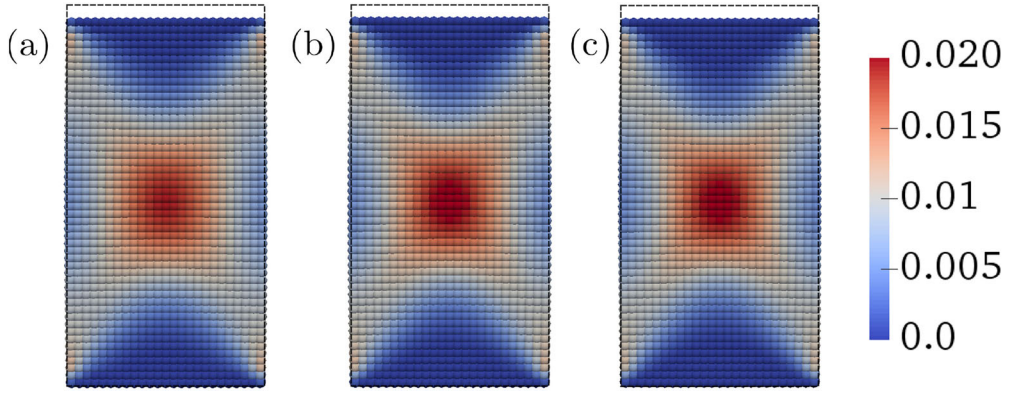

Figure 14. Contours of equivalent plastic shear strain at the applied peak load for (a) $v_y = 0.003$ mm/s, (b) $v_y = 0.006$ mm/s, and (c) $v_y = 0.009$ mm/s, respectively.

volumetric strains as well as water pressures at two loading steps, as shown by the vertical dash lines in Figure 13. Figures 14 and 15 plot the contours of the equivalent plastic shear strain for all cases at the peak reaction force and in the post-localised regime, respectively. Similarly, Figures 16 and 17 present the contours of plastic volumetric strains at the two load steps, respectively. The results in Figures 14 and 16 show that the plastic strains are similar at the peak reaction force for the three loading rates. As shown in Figures 15 and 17, the increase of loading rate generates a slight increase of both shear and volumetric plastic strains in the shear bands. This observation is corroborated by the loading capacity curves in Figure 13.

Figures 18 and 19 portray the contours of water pressure on the deformed configuration for the three loading rates at two vertical compressions in Figure 13, respectively. The results in Figure 18 show that no obvious banded zone of water pressure forms in the specimen at the peak applied load. However, the smaller loading rate (longer physical time for the same vertical compression) generates larger pore water pressure (smaller matric suction) in the specimen under the same vertical compression. In the post-localised loading regime, as shown in Figure 19, larger matric suction is generated inside and

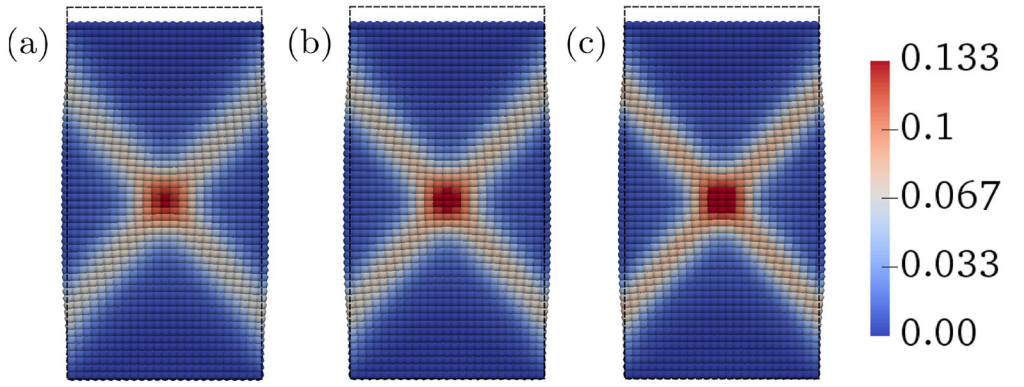

Figure 15. Contours of equivalent plastic shear strain in the post-localisation regime for (a) $v_y = 0.009$ mm/s, (b) $v_y = 0.006$ mm/s, and (c) $v_y = 0.009$ mm/s, respectively.

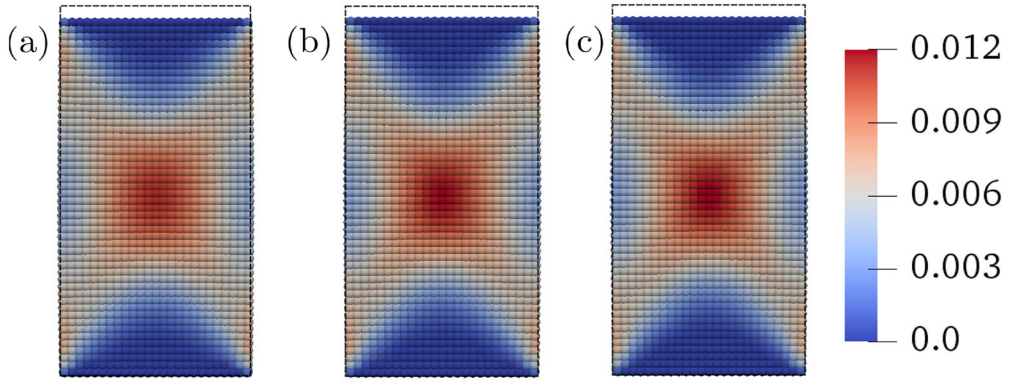

Figure 16. Contours of plastic volumeteric strain at the applied peak load for (a) $v_y = 0.003$ mm/s, (b) $v_y = 0.006$ mm/s, and (c) $v_y = 0.009$ mm/s, respectively.

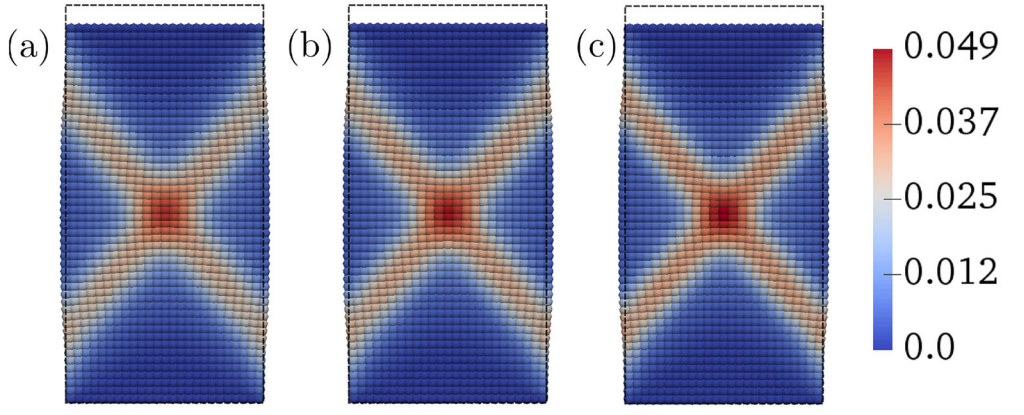

Figure 17. Contours of plastic volumetric strain in the post-localisation regime for (a) $v_y = 0.003$ mm/s, (b) $v_y = 0.006$ mm/s, and (c) $v_y = 0.009$ mm/s, respectively.

outside the shear band for the simulation with a larger loading rate. This may explain why the loading capacity is larger for the simulation with a larger loading rate because a larger matric suction generally increases the overall strength of unsaturated soils (Lu & Likos, 2004). Similarly, the observed bifurcations

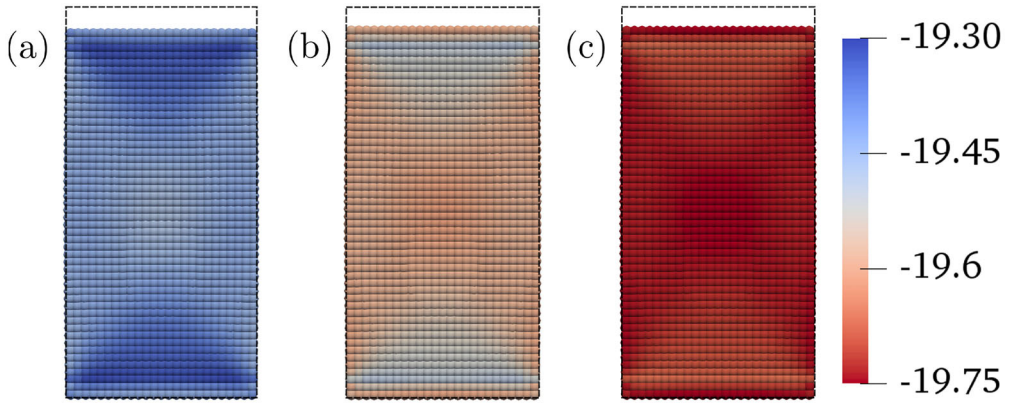

Figure 18. Contours of water pressure (unit: kPa) at the applied peak load for (a) $v_y = 0.003$ mm/s, (b) $v_y = 0.006$ mm/s, and (c) $v_y = 0.009$ mm/s, respectively.

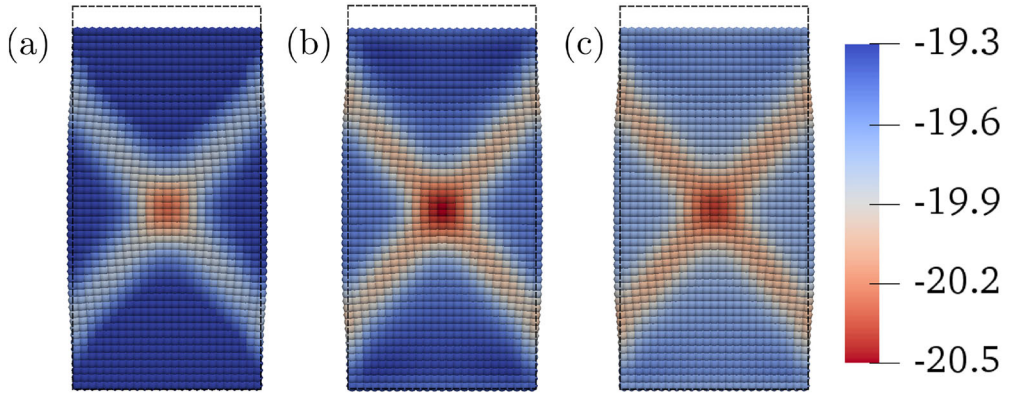

Figure 19. Contours of water pressure (unit: kPa) in the post-localisation regime for (a) $v_y = 0.003$ mm/s, (b) $v_y = 0.006$ mm/s, and (c) $v_y = 0.009$ mm/s, respectively.

of the load capacity curves in Figures 6 and 13 may be due to the different variations of matric suctions in the unsaturated soil specimen under different length scale or loading rate scenarios.

4. Conclusions

This article focuses on studying the impact of spatial length scales and loading rates on the formation of shear bands in unsaturated geomaterials through a fully coupled nonlocal hydromechanical model. For the purpose, we present a strong nonlocal hydromechanical model formulated based on state-based peridynamics for simulating strain localisation in unsaturated geomaterials assuming passive atmospheric pressure (i.e. zero air pressure). The governing equations are integro-differential equations in which length scales are assumed for both the skeleton deformation and pore fluid flow. Numerical simulations of shear bands in unsaturated geomaterials were conducted to investigate the impact of the spatial length scale and the mechanical loading rate on the formation of shear bands. The numerical results have shown that both the deformation and negative pore water pressure are concentrated in the shear bands with a finite thickness. The preliminary results have demonstrated that both the length scale and the mechanical loading rate affect the formation of shear bands in unsaturated geomaterials as well as the peak value of the load capacity of such materials.

Acknowledgement

The authors are grateful to the two anonymous reviewers for their constructive reviews of this article.

Disclosure statement

No potential conflict of interest was reported by the authors.

Funding

The research was supported by the US National Science Foundation under Contract numbers CMMI - 1659932 and 1944009.

References

Andò, E., Hall, S. A., Viggiani, G., Desrues, J., & Bésuelle, P. (2012). Grain-scale experimental investigation of localised deformation in sand: a discrete particle tracking approach. *Acta Geotechnica*, *7*(1), 1–13. https://doi.org/10.1007/s11440-011-0151-6

Askrinejad, A., Casini, F., Bischof, P., Beck, A., & Springman, S. (2012). Rainfall induced instabilities: A field experiment on a silty sand slope in Northern Switzerland. *Rivista Italiana Di Geotecnica*, *3*(1), 50–71.

Borja, R. I. (2004). Cam-clay plasticity. Part V: A mathematical framework for three-phase deformation and strain localization analyses of partially saturated porous media. *Computer Methods in Applied Mechanics and Engineering*, *193*(48–51), 5301–5338. https://doi.org/10.1016/j.cma.2003.12.067

Borja, R. I., Song, X., Rechenmacher, A. L., Abedi, S., & Wu, W. (2013). Shear band in sand with spatially varying density. *Journal of the Mechanics and Physics of Solids*, *61*(1), 219–234. https://doi.org/10.1016/j.jmps.2012.07.008

Borja, R. I., Song, X., & Wu, W. (2013). Critical state plasticity. Part VII: Triggering a shear band in variably saturated porous media. *Computer Methods in Applied Mechanics and Engineering*, *261–262*, 66–82. https://doi.org/10.1016/j.cma.2013.03.008

Cao, J., Jung, J., Song, X., & Bate, B. (2018). On the soil water characteristic curves of poorly graded granular materials in aqueous polymer solutions. *Acta Geotechnica*, *13*(1), 103–116. https://doi.org/10.1007/s11440-017-0568-7

Chang, C. S., Hicher, P.-Y., & Daouadji, A. (2009). Investigating instability in granular materials by means of a microstructural model. *European Journal of Environmental and Civil Engineering*, *13*(2), 167–186. https://doi.org/10.1080/19648189.2009.9693098

Desrues, J., Chambon, R., Mokni, M., & Mazerolle, F. (1996). Void ratio evolution inside shear bands in triaxial sand specimens studied by computed tomography. *Géotechnique*, *46*(3), 529–546. https://doi.org/10.1680/geot.1996.46.3.529

Ehlers, W., Ramm, E., Diebels, S., & d'Addetta, G. (2003). From particle ensembles to cosserat continua: homogenization of contact forces towards stresses and couple stresses. *International Journal of Solids and Structures*, *40*(24), 6681–6702. https://doi.org/10.1016/S0020-7683(03)00418-9

Jrad, M., Sukumaran, B., & Daouadji, A. (2012). Experimental analyses of the behaviour of saturated granular materials during axisymmetric proportional strain paths. *European Journal of Environmental and Civil Engineering*, *16*(1), 111–120. https://doi.org/10.1080/19648189.2012.666900

Li, C., & Laloui, L. (2017). Coupled thermo-hydro-mechanical effects on caprock stability during carbon dioxide injection. *Energy Procedia*, *114*, 3202–3209. https://doi.org/10.1016/j.egypro.2017.03.1683

Likos, W. J., Song, X., Xiao, M., Cerato, A., & Lu, N. (2019). Fundamental challenges in unsaturated soil mechanics. In *Geotechnical fundamentals for addressing new world challenges* (pp. 209–236). Springer.

Lu, N., Godt, J. W., & Wu, D. T. (2010). A closed-form equation for effective stress in unsaturated soil. *Water Resources Research*, *46*(5). https://doi.org/10.1029/2009WR008646

Lu, N., & Likos, W. J. (2004). *Unsaturated soil mechanics*. Wiley.

Menon, S., & Song, X. (2019). Coupled analysis of desiccation cracking in unsaturated soils through a nonlocal mathematical formulation. *Geosciences*, *9*(10), 428. https://doi.org/10.3390/geosciences9100428

Niu, W.-J., Ye, W.-M., & Song, X. (2020). Unsaturated permeability of gaomiaozi bentonite under partially free-swelling conditions. *Acta Geotechnica*, *15*, 1095–1124.

Pardoen, B., Levasseur, S., & Collin, F. (2015). Using local second gradient model and shear strain localisation to model the excavation damaged zone in unsaturated claystone. *Rock Mechanics and Rock Engineering*, *48*(2), 691–714. https://doi.org/10.1007/s00603-014-0580-2

Rattez, H. (2017). *Thermo-hydro-mechanical couplings and strain localization in Cosserat continua: application to stability analysis of rapid shear in faults* [PhD thesis].

Silling, S. A. (2000). Reformulation of elasticity theory for discontinuities and long-range forces. *Journal of the Mechanics and Physics of Solids*, *48*(1), 175–209. https://doi.org/10.1016/S0022-5096(99)00029-0

Silling, S. A., & Askari, E. (2005). A meshfree method based on the peridynamic model of solid mechanics. *Computers & Structures*, *83*(17-18), 1526–1535. https://doi.org/10.1016/j.compstruc.2004.11.026

Silling, S. A., Epton, M., Weckner, O., Xu, J., & Askari, E. (2007). Peridynamic states and constitutive modeling. *Journal of Elasticity*, *88*(2), 151–184. https://doi.org/10.1007/s10659-007-9125-1

Song, X. (2014). *Strain localization in unsaturated porous media* [PhD thesis]. Stanford University.

Song, X. (2017). Transient bifurcation condition of partially saturated porous media at finite strain. *International Journal for Numerical and Analytical Methods in Geomechanics*, *41*(1), 135–156. https://doi.org/10.1002/nag.2552

Song, X., & Borja, R. I. (2014a). Finite deformation and fluid flow in unsaturated soils with random heterogeneity. *Vadose Zone Journal*, *13*(5), 0131. https://doi.org/10.2136/vzj2013.07.0131

Song, X., & Borja, R. I. (2014b). Mathematical framework for unsaturated flow in the finite deformation range. *International Journal for Numerical Methods in Engineering*, *97*(9), 658–682. https://doi.org/10.1002/nme.4605

Song, X., & Khalili, N. (2019). A peridynamics model for strain localization analysis of geomaterials. *International Journal for Numerical and Analytical Methods in Geomechanics*, *43*(1), 77–96. https://doi.org/10.1002/nag.2854

Song, X., & Menon, S. (2019). Modeling of chemo-hydromechanical behavior of unsaturated porous media: a nonlocal approach based on integral equations. *Acta Geotechnica*, *14*(3), 727–747. https://doi.org/10.1007/s11440-018-0679-9

Song, X., & Silling, S. (2019). On the peridynamic effective force state and multiphase correspondence principle. *Journal of the Mechanics and Physics of Solids*, Revision in review, 1–30.

Song, X., Wang, K., & Bate, B. (2018). A hierarchical thermo-hydro-plastic constitutive model for unsaturated soils and its numerical implementation. *International Journal for Numerical and Analytical Methods in Geomechanics*, *42*(15), 1785–1805. https://doi.org/10.1002/nag.2811

Song, X., Wang, K., & Ye, M. (2018). Localized failure in unsaturated soils under non-isothermal conditions. *Acta Geotechnica*, *13*(1), 73–85. https://doi.org/10.1007/s11440-017-0534-4

Song, X., Ye, M., & Wang, K. (2017). Strain localization in a solid-water-air system with random heterogeneity via stabilized mixed finite elements. *International Journal for Numerical Methods in Engineering*, *112*(13), 1926–1950. https://doi.org/10.1002/nme.5590

Van Genuchten, M. T. (1980). A closed-form equation for predicting the hydraulic conductivity of unsaturated soils 1. *Soil Science Society of America Journal*, *44*(5), 892–898. https://doi.org/10.2136/sssaj1980.03615995004400050002x

Wang, K., & Song, X. (2020). Strain localization in non-isothermal unsaturated porous media considering material heterogeneity with stabilized mixed finite elements. *Computer Methods in Applied Mechanics and Engineering*, *359*, 112770. https://doi.org/10.1016/j.cma.2019.112770

Zhang, H., & Schrefler, B. (2004). Particular aspects of internal length scales in strain localization analysis of multiphase porous materials. *Comput Meth Appl Mech Eng*, *193*(27–29), 2867–2884. https://doi.org/10.1016/j.cma.2003.11.012

Zienkiewicz, O. C., Chan, A., Pastor, M., Schrefler, B., & Shiomi, T. (1999). *Computational geomechanics*, volume 613. Citeseer.